33RD CONGRESS
OF THE INTERNATIONAL COUNCIL
OF THE AERONAUTICAL SCIENCES
STOCKHOLM, SWEDEN, 4–9 SEPTEMBER, 2022

ICAS
2022
SWEDEN

REACTIVE CONTROL OF BYPASS TRANSITION IN A WING BOUNDARY LAYER

José M. Faúndez Alarcón[1], Kenzo Sasaki[1], Ardeshir Hanifi[1], Roger Larsson[2] & Dan S. Henningson[1]

[1]KTH Royal Institute of Technology, Linné FLOW Centre, SE-10044, Stockholm, Sweden
[2]Saab Aeronautics, Bröderna Ugglas gata, SE-58188, Linköping, Sweden

Abstract

This investigation deals with the numerical implementation of a data-driven method for reactive control of the boundary-layer over a NACA0008 airfoil. The aim of this work is to evaluate the performance of controller in damping the flow disturbances and its efficiency in delaying laminar-turbulent transition. We focus our attention on the bypass transition scenario caused by free-stream turbulence. In this scenario, the perturbations in the wing boundary-layer develop into streaky structures. We show that this data-driven method is effective in decreasing the wall shear stress and disturbance energy at the objective location, and this damping is sustained downstream of the objective location. However, further downstream, the fluctuations grow again reaching amplitudes similar to those in the uncontrolled case.

Keywords: Flow control, Bypass transition.

1. Introduction

In wall-bounded flows, the skin friction is attributed to be one of the major sources of drag due to the turbulent state that the flow goes through [1]. For this reason, maintaining a laminar boundary layer, with its lower skin friction, is of great interest in many application where savings in fuel consumption and reduction in emissions are sought, such as commercial aircraft transportation. Depending on the speed regime and geometry of an aircraft, laminar flow can be maintained either by Natural Laminar Flow (NLF) design or by Hybrid Laminar Flow Control (HLFC). By increasing the area of the wing that is laminar, as can be seen in Figure 1, the potential drag reduction can be about 28% on the wing, which gives a reduction of about 5% of the total aircraft drag for a typical subsonic cruise condition.
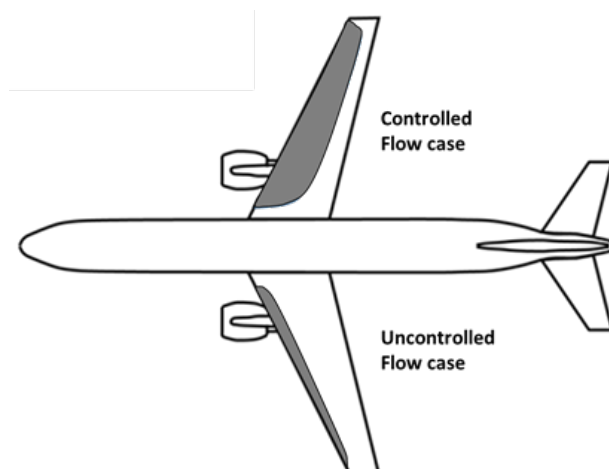

Figure 1 – Potential difference in laminar wing area (grey) between uncontrolled and controlled flow.

The route from laminar to turbulent state in the wall-bounded flows is not unique. When a two-dimensional boundary layer is forced by free-stream disturbances of sufficient large amplitude, the

transition scenario deviates from the classical route characterised by the amplification and break-down of the unstable eigenmodes known as Tollmien-Schlichting (TS) waves [2]. In this high-level disturbance situation, the perturbed flow exhibits streamwise-elongated structures of alternating high and low streamwise velocity. These streaky structures grow in amplitude as they propagate down-stream, and once they reach a high enough amplitude they undergo secondary instabilities followed by the nucleation and growth of turbulent spots. This process is commonly referred to as bypass transition and is a characteristic of the boundary layer flows forced by free-stream turbulence (FST). The broadband nature of FST makes this scenario highly intermittent, with the random appearance of turbulent spots in space and time.

In the present work, we study numerically the control of streaky structures and its efficiency in delay-ing transition to turbulence in the boundary-layer over a NACA0008 profile, corresponding to the wing model manufactured by Saab and used in experiments at KTH and ITA (see, e.g., [3]). The aim of this work is to use a data-driven approach with the potential of being also applied in an experimental investigation, where the flow information will be limited to a wall measurements at a discrete number of locations. To this end, we follow the method already implemented in previous investigations [4, 5], where zero pressure gradient boundary layers were considered, and develop a control law that can later be tested as a proof of concept on the real wing in a wind tunnel.

2. Governing equations

In this work, the incompressible Navier-Stokes equations for unsteady flows are solved numerically. In non-dimensional form they read

$$\frac{\partial \mathbf{q}}{\partial t} + (\mathbf{q} \cdot \nabla)\mathbf{q} = -\nabla p + \frac{1}{Re}\nabla^2 \mathbf{q} + \mathbf{f}, \tag{1}$$

$$\nabla \cdot \mathbf{q} = 0, \tag{2}$$

where $\mathbf{q} = (v_{x_1}, v_{x_2}, v_{x_3})$ represents the velocity vector in the Cartesian coordinates $\mathbf{x} = (x_1, x_2, x_3)$, p the pressure, $\mathbf{f}$ the forcing and Re the Reynolds number based on the chord length and free-stream velocity, which in our simulations is set to $Re = 5.333 \times 10^5$. Given the curvature of the wing, some of the results will be presented in terms of the wall-normal coordinate n. The equations are solved using the spectral-element code `Nek5000` [6], where a polynomial order $N = 8$ is used.

3. Flow Configuration

The airfoil geometry used in this investigation corresponds to a NACA0008 profile at zero angle of attack, where only a section around the leading-edge is considered to save computational time. For all the simulations, non-slip boundary conditions are imposed at the airfoil surface, outflow at the end of the domain, and Dirichlet boundary condition in the free-stream. Note that periodicity is imposed in the spanwise direction.

Free-stream turbulence is synthesised and introduced in the domain by superimposing Fourier modes as Dirichlet boundary condition at the inflow boundary following the method used by [7]. 1600 Fourier modes are randomly selected and given an energy according to the Von-Kármán spectrum

$$E(k) = \frac{2}{3}\frac{1.606(kL)^4}{[1.350 + (kL)^2]^{17/6}}Lq, \tag{3}$$

with L being the turbulence integral length scale, k the total wavenumber, and $q = 3/2(Tu)^2$ the total turbulent kinetic energy. In all of our simulations presented here, a value of $L = 0.01$ has been used. In figure 2, a snapshot of the flow field is presented showing the streamwise velocity perturbation. Here, it is highlighted how the perturbations inside the boundary layer develop into the streaky struc-tures of alternating low and high speed, while in the free-stream the perturbations maintain their random behaviour.

The actuators are modelled in the numerical simulations as body forces $\mathbf{f}_u$ in equation (1) as

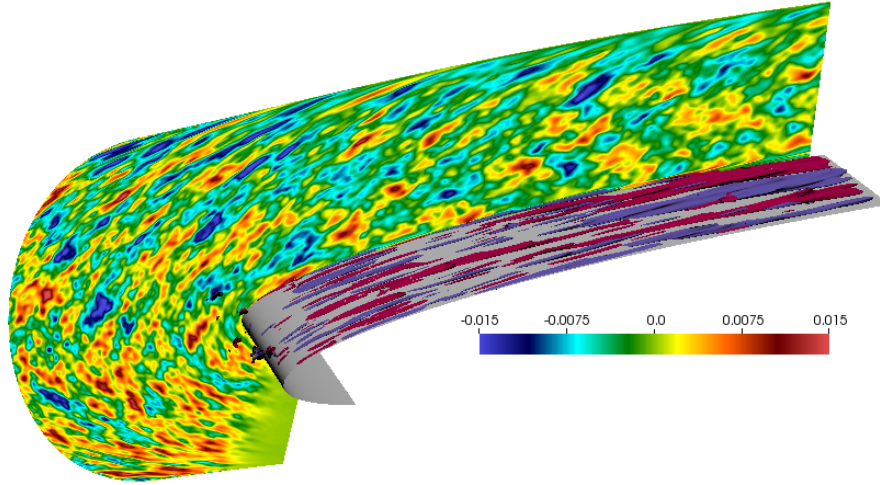$$\mathbf{f}_u(\mathbf{x}) = u(t)\mathbf{b}(\mathbf{x}), \tag{4}$$

Figure 2 – Snapshot of the flow field. Streaky structures are shown as isosurfaces of streamwise velocity perturbation of ± 0.01.

where $\mathbf{b}(\mathbf{x})$ corresponds to the spatial support of the forcing in the domain, while $u(t)$ to the actuation signal that modulates the forcing in time and is given by the control law. The actuators have a Gaussian shape centred at $\mathbf{x}_u$, with a component in the wall normal direction. Although these actuators do not match any physical actuator, the idea behind of the use of a body force is to mimic the effect that a plasma actuator has on the flow field [8].

4. Control law

Figure 3a depicts the schematic of the plant for the control design and implementation. The actuation decision is based on localised sensors at the wall, measuring an average of the streamwise shear stress variations

$$y(t) = \frac{1}{S} \int_S \frac{\partial v_t}{\partial n} \mathrm{d}S, \tag{5}$$

where S corresponds to the area of the sensor, and the subscript t denotes the velocity component in the streamwise direction and tangent to the wing surface. The choice of shear-stress measurements comes from the estimation results by [9]. In that investigation, they tested shear-stress and pressure measurements at the wall, concluding that the best estimation for streaks comes from the use of the former, since pressure measurements are highly influenced by free-stream fluctuations. These shear-stress sensors have also been used in the previous flat-plate simulations by [5, 4] for the same purpose.

Since the flow is convective, we adopt a feed-forward configuration by placing the actuators downstream of the measurements $y(t)_l$, yielding an actuation signal of the form

$$u(t)_m = \int_0^t \sum_{l=1}^{N_y} k_l(t - \tau) y(\tau)_l \mathrm{d}\tau. \tag{6}$$

Here, $N_y = 20$ denotes the number of sensors $y(t)_l$ along the span. Further, the subscript m represents the $N_u = 20$ actuators also distributed uniformly along the span. Note that the number of sensors at the objective location is also 20. The kernel k_l in equation (6) is defined by the control law, which for this work corresponds to the inversion feed-forward control (IFFC). This technique is designed in the frequency domain based on the open-loop transfer functions $\hat{G}^{uz}$, from the actuation $u(t)_m$ to the objective sensors $z(t)_l$, and $\hat{G}^{yz}$, corresponding to the estimation of $z(t)_l$ from the reference $y(t)_l$. The relative location of sensors and actuators, with their respective open-loop transfer functions, is shown in figure 3b. Given the periodicity along the span and assuming a linear system, an estimation of the objective measurements $\hat{z}(\omega, \beta)$ can be obtained from

$$\hat{z}(\omega, \beta) = \hat{G}^{uz}(\omega, \beta)\hat{u}(\omega, \beta) + \hat{G}^{yz}(\omega, \beta)\hat{y}(\omega, \beta), \tag{7}$$

where ω and β correspond to the angular frequency and the spanwise wavenumber, respectively, while the hat represents the quantities in frequency domain.
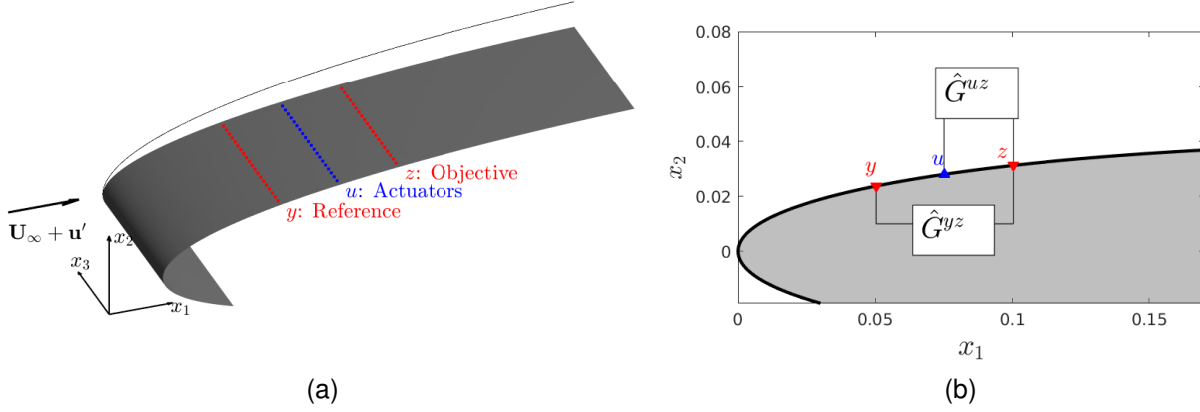

(a)   (b)

Figure 3 – Schematic of the control configuration showing the sensors (red) and actuators (blue) placement, together with the transfer function between them.

The objective of the controller is the complete cancellation of the objective $\hat{z}$ by the actuation $\hat{u} = \hat{K}\hat{y}$. This becomes an $\mathscr{H}_2$ optimal control problem [10] with solution given by

$$\hat{K} = \frac{\left(\hat{G}^{uz}\right)^H \hat{Q}\hat{G}^{yz}}{\hat{R} + \left(\hat{G}^{uz}\right)^H \hat{Q}\hat{G}^{uz}}, \tag{8}$$

where $\hat{Q}$ and $\hat{R}$ are weights to be chosen. Finally, the inverse Fourier transform of $\hat{K}$ leads to the kernel as in equation (6). The kernel is designed offline based on the wall measurements from uncontrolled simulations. The steps involved in this process are detailed in the next section. Once the kernel is available, we can perform the simulations of flow control where the actuation signal $u(t)_m$, as in equation 6, is obtained from the actual measurements of the sensors $y(t)_l$.

4.1 Transfer functions

The offline design of the control kernel is performed from the sensors signals obtained using two different numerical simulations. As it was shown in equation (8), this design is based on the knowledge of two transfer functions, namely $\hat{G}^{yz}$ and $\hat{G}^{uz}$. The former is the computationally most demanding part of the design since it is constructed from the signals of an uncontrolled case. Once the time-series are collected, the optimal frequency response can be computed as [11]

$$\hat{G}^{yz} = \frac{\hat{S}_{yz}}{\hat{S}_{yy}}, \tag{9}$$

with $\hat{S}_{yz}$ and $\hat{S}_{yy}$ denoting the cross- and auto-spectra, respectively. $\hat{S}_{yz}$ and $\hat{S}_{yy}$ are obtained through ensemble averages using the Welch method and by considering 8 bins with 50% of overlap. Then, the impulse response, which by definition corresponds to the transfer function in physical domain, is computed as the inverse Fourier transform of 9. This is, of course, based on the assumption that the system $y \rightarrow z$ is stable and physically realisable [11]. Stability is confirmed by checking that the signals are bounded, while the system being physically realisable is a consequence of the relative position of the sensors y and z and the convective characteristic of the flow. As an example, figure 4a shows the prediction of one sensor $z(t)_l$ from the reference $y(t)_l$ by using the open-loop transfer function obtained from equation (9). The real measurements are also included in figure 4a, showing a good agreement with the prediction.
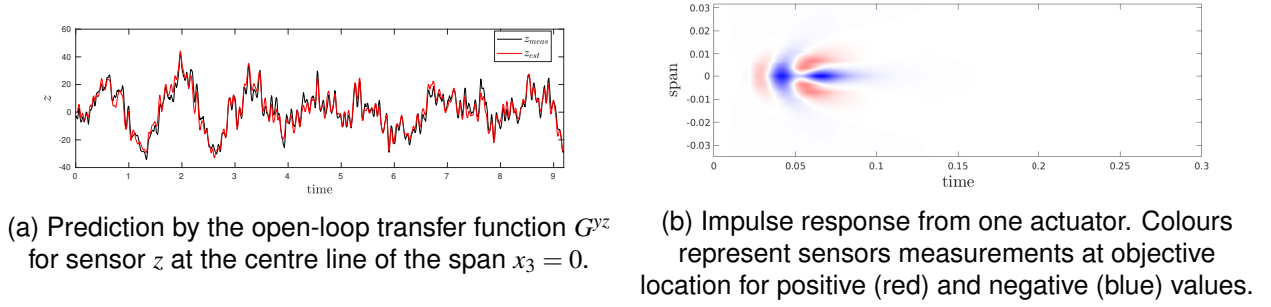
(a) Prediction by the open-loop transfer function G^{yz} for sensor z at the centre line of the span $x_3 = 0$.

(b) Impulse response from one actuator. Colours represent sensors measurements at objective location for positive (red) and negative (blue) values.

Figure 4 – Transfer functions needed for the kernel design.

On the other hand, the transfer function $\hat{G}^{uz}$ is obtained via the Fourier transform of the finite impulse response from the actuators to the sensors $z(t)_l$. Given the periodicity of the domain, and the fact the all actuators are identical, only one impulse response from a single actuator to all sensors at the objective location is required, as it was shown in [12]. The impulse response from the centre actuator is shown in figure 4b. The kernel is then computed from these two transfer function as in equation (8) and its inverse Fourier transform can then be implemented in the non-linear simulations. Here, the weights in equation (8) are selected offline based on the signal analysis and such that maximum reduction of the objective measurements is achieved.

5. Results

Here, different flow and control configurations have been considered. A low free-stream turbulence environment was simulated to evaluate the capability of the controller in cancelling linear streaks, considering that only wall measurements are performed. The free-stream turbulence intensity was then increased to promote the generation of turbulent spots within our numerical domain. For this higher turbulence intensity situation, we evaluated two different chord locations for placement of sensors/actuators. The parameters of the configurations under these studies are presented in table 1.

Table 1 – List of simulations with their respective turbulence intensities and sensors ($x_{1,y}$, $x_{1,z}$) and actuators ($x_{1,u}$) locations.

Case	Tu (%)	$x_{1,y}$	$x_{1,u}$	$x_{1,z}$
Low turbulence	0.5	0.05	0.075	0.10
Controller 1	2.5	0.05	0.075	0.10
Controller 2	2.5	0.10	0.125	0.15

The absolute and relative chord location of sensors and actuators in table 1 are not optimal in a mathematical sense. They are based on the following considerations

- The whole control unit should be upstream of the nucleation of turbulent spots, where the actuators can actually act on the streaky structures before they undergo a secondary instability. Moreover, non-linear effects become more important downstream, affecting the performance of the transfer function in equation 9.

- The control unit should also be far enough downstream of the leading edge to allow the development of streaks, where the boundary-layer has already filtered out the frequencies and wavenumbers that cannot experience high transient growth downstream.

- The distance between the sensors $y(t)_l$ and $z(t)_l$ should be enough to place the actuators in between them (see, for instance, the work by [8] where the body forces had an extension of $\approx 4[mm]$). However, increasing their spacing deteriorates the performance of the estimation transfer function in equation 9.

- The placement of the actuators in the mid point between of the rows of sensors responds to the trade-off between the efficiency and performance of the controller. By placing the actuators closer to the $y(t)_l$ sensors, the actuation disturbances can reach a higher growth at the objective location, resulting in a more efficient actuation. However, this distance is limited by two factors that directly affect the performance of the controller. First, an undesirable feedback to the sensors $y(t)_l$. And second, the time that the actuation disturbances take to the objective location increases, meaning that they may be not fast enough to cancel the incoming disturbances detected by $y(t)_l$. The consequence of this in our approach is a control kernel with a significant non-causal part, requiring future measurements for actuation. This is well-known drawback of the IFFC and some discussions about it can be found in [3, 4].

5.1 Low turbulence case

After running the uncontrolled simulation to design the open-loop transfer functions described before, we build the control kernel for this low turbulence case. The span and time distribution of the kernel is presented in figure 5a, showing how it is concentrated around $t = 0$ and with a weight at the centre of the kernel (span$= 0$).

The final step is the implementation of the designed kernel and the evaluation of its performance in the numerical simulation. The first metric under consideration is the amplitude of the objective function given by $z(t)_l$, being the quantity to be minimised by the control law. Since the quantity to be minimised corresponds to signals from a row of sensors, figure 5b shows the mean-squared along the span. Here, it can be seen how the shear-stress fluctuations at the location of sensors z_l decrease when the control is active.
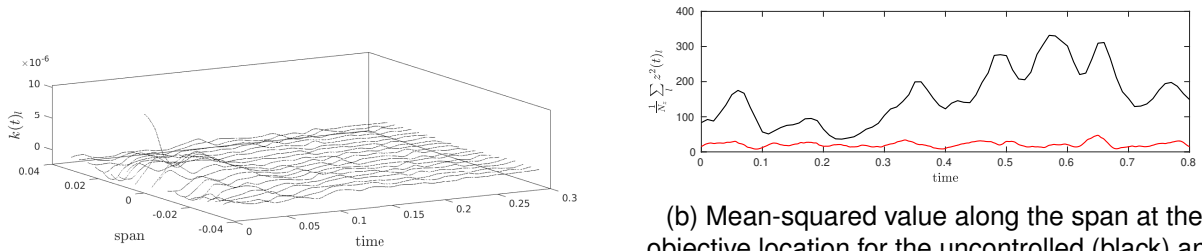
(a) Control kernel for case corresponding to $Tu = 0.5\%$.

(b) Mean-squared value along the span at the objective location for the uncontrolled (black) and uncontrolled (red) cases.

Figure 5 – Control kernel (a) and its performance (b) in the numerical simulation.

As mentioned before, the controller is designed using wall-measurements only. This, of course, introduces a limitation in the definition of the control objective function, which can only be based on the wall signals, while our main goal is the damping of energy of streaks. In order to assess the merit of the shear-stress as a useful quantity for our purposes, we monitor the wall-normal distribution of the r.m.s. streamwise velocity at several chord locations (see figure 6). Given the convective nature of the flow, the profiles are identical before the actuation location at $x_1 = 0.075$. Then, after a small increase at the actuation location, the amplitude of the streaks decays downstream.
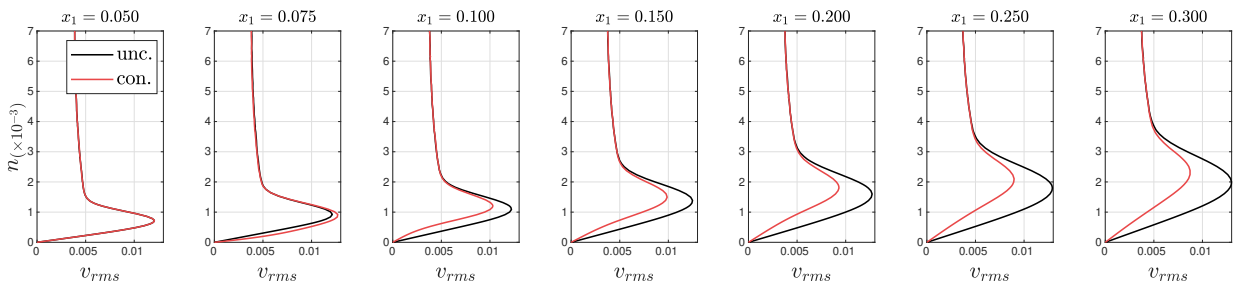

Figure 6 – Wall-normal distribution of the r.m.s. streamwise velocity at different chord locations.

5.2 High turbulence cases

Using the same techniques, we designed the control kernels, as in equation 6, for the cases with turbulence intensity of 2.5%. Here, the appearance and evolution of turbulent spots can be observed within our numerical domain, and therefore the controller capability in delaying bypass transition can be assessed. For this case, and in addition to the controller with sensors and actuators presented in figure 3b, a second controller was introduced. These two control units are listed in table 1 as 'Controller 1' and 'Controller 2', where Controller 2 is placed $\Delta x_1 = 0.05$ downstream of Controller 1. Figure 7 depicts the two control kernels built for this case, showing a similar shape with respect to the low free-stream turbulence case.

(a) Controller 1   (b) Controller 2
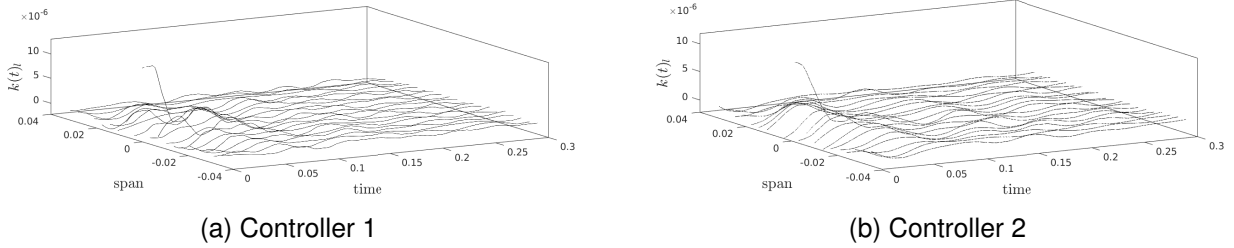
Figure 7 – Control kernels for cases corresponding to $Tu = 2.5\%$.

Similar to the low free-stream turbulence case, the kernels were designed offline and then tested in DNS. The mean-squared of $z(t)_l$ signals along the span is presented in figure 8. For both cases it can be noted how the signal amplitudes at the objective location decrease when the actuators are active. This reduction is significant after $\Delta t \approx 0.1$ from the beginning of the plot, which corresponds to the time extension where the control kernels are concentrated (see figure 7). To evaluate the performance of the controller we define the performance index

$$\mathscr{E} = 1 - \frac{\mathscr{J}_{con}}{\mathscr{J}_{unc}} \quad , \text{with} \quad \mathscr{J} = \sum_{l=1}^{N_z} \int_{t_0}^{t_f} z(t)_l^2 \mathrm{d}t, \tag{10}$$

obtaining a performance of 0.632 and 0.568 for Controller 1 and 2, respectively, which are close to the values obtained during the offline design process.
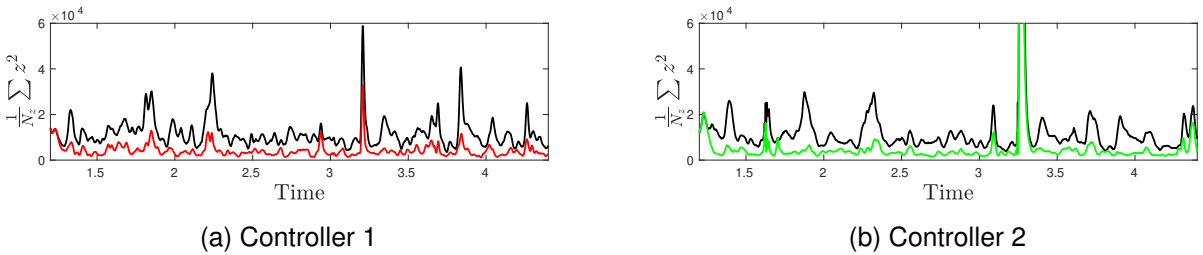

(a) Controller 1   (b) Controller 2

Figure 8 – Time evolution of the mean squared signal along the span for the uncontrolled (black lines) and controlled (colour lines) cases .

Since the controllers are working as expected in decreasing the objective function, we can now evaluate their performance regarding streaks damping and the effect in maintaining a laminar flow state. To this end, statistics are computed based on the signal length presented in figure 8, which corresponds roughly to five flow-through (~ 0.6 time unit) after discarding the first 0.6 time units. The length of this series is not long enough to have converged statistics, however it is considered to be enough to assess the control performance. This is mainly due to three reasons. First, the fact that the whole transition phenomenon can be observed within this time length, where the growth, instability, and breakdown of streaks take place. Second, as can be seen in figure 7, the kernels have an extension of 0.3 time unit, being most of their weight concentrated in $t < 0.1$. Finally, the comparison between the different cases is made considering the same physical time, and where the random

seed used to generate the free-stream turbulence was fixed, allowing us a one-to-one comparison between them.

Figure 9 shows the peak of the r.m.s. streamwise velocity along the chord. Here, it can be noted how the disturbance amplitude is reduced at the corresponding objective location ($x_1 = 0.1$ for Controller 1 and $x_1 = 0.15$ for Controller 2), with a peak reduction of 17.6% and 11.7% for Controller 1 and 2, respectively. The damping of the streaks is still noticeable after the actuation and objective locations, but further downstream the disturbances 'recover' their growth, following the one of the uncontrolled case. A similar behaviour has been reported in previous experimental and numerical investigations [13, 9], where one of the explanations for the fast growth downstream was the entry of new disturbances from the free-stream turbulence.
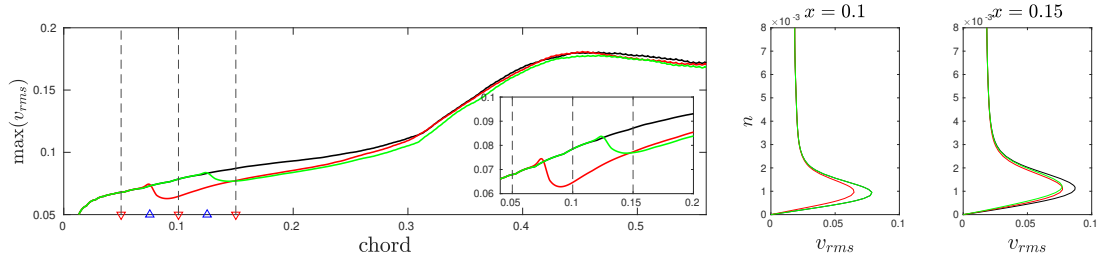

Figure 9 – Evolution of the wall-normal maximum r.m.s. streamwise velocity along the chord. The streamwise velocity profiles at the objective location are also included. Lines colours are the same as in figure 8. Red and blue triangles represent the location of sensors and actuators, respectively.

To shed light on the effect of the controller on the objective function, the spectrum of the perturbation energy is computed. This is done by taking the discrete Fourier transform of the velocity perturbation in time and along the span. Then, for each pair (ω, β) and a given chord location the energy is computed as

$$E(x_1, \omega, \beta) = \frac{1}{2} \int_0^{3\delta^*} \left(|\hat{v}_{x_1}|^2 + |\hat{v}_{x_2}|^2 + |\hat{v}_{x_3}|^2 \right) \mathrm{d}n, \tag{11}$$

with δ^* being the local displacement thickness. The discrete spectra are presented in figure 10 for the uncontrolled and controlled cases at their corresponding objective locations. From these plots, it can be seen that the most energetic components are damped when the controllers are active, where the peaks (in yellow) fade in the plots for the controlled cases. These results not only confirm that the controller is effective in minimising the objective function, as it was shown in figure 8, but also show that it does so by acting on the most amplified frequencies and wavenumbers at the objective location.

The reason behind the poor performance of the controller in delaying bypass transition is the object of our ongoing investigations. Our preliminary results suggest that in our flow configuration the streaks responsible for transition are not the most energetic disturbances in a statistical sense. This is consistent with the random appearance of turbulent spots within the domain. Part of the justification for this claim comes from the visual inspection of the flow fields. In figure 11, we present snapshots of the flow field for the uncontrolled and the Controller 2 cases at the same time instants. The location of two turbulent spots are marked in the bottom plots. Even though the effect of the controller after the objective location can be noticed, the same turbulent spots appear downstream. To elucidate the effect of the controller on these disturbances, the turbulent spots are traced back in time to see their initial characteristics closer to the objective location. We note that they are initiated from narrow low-speed streaks, being present in the controlled and uncontrolled snapshots. As can be seen there, the controller seems to have no effect on these structures. The same development has been observed for other turbulent spots in the flow field. Consequently, our current efforts are concentrated in the characterisation of the early stages of these turbulent spots to redefine our method and act more effectively on them.

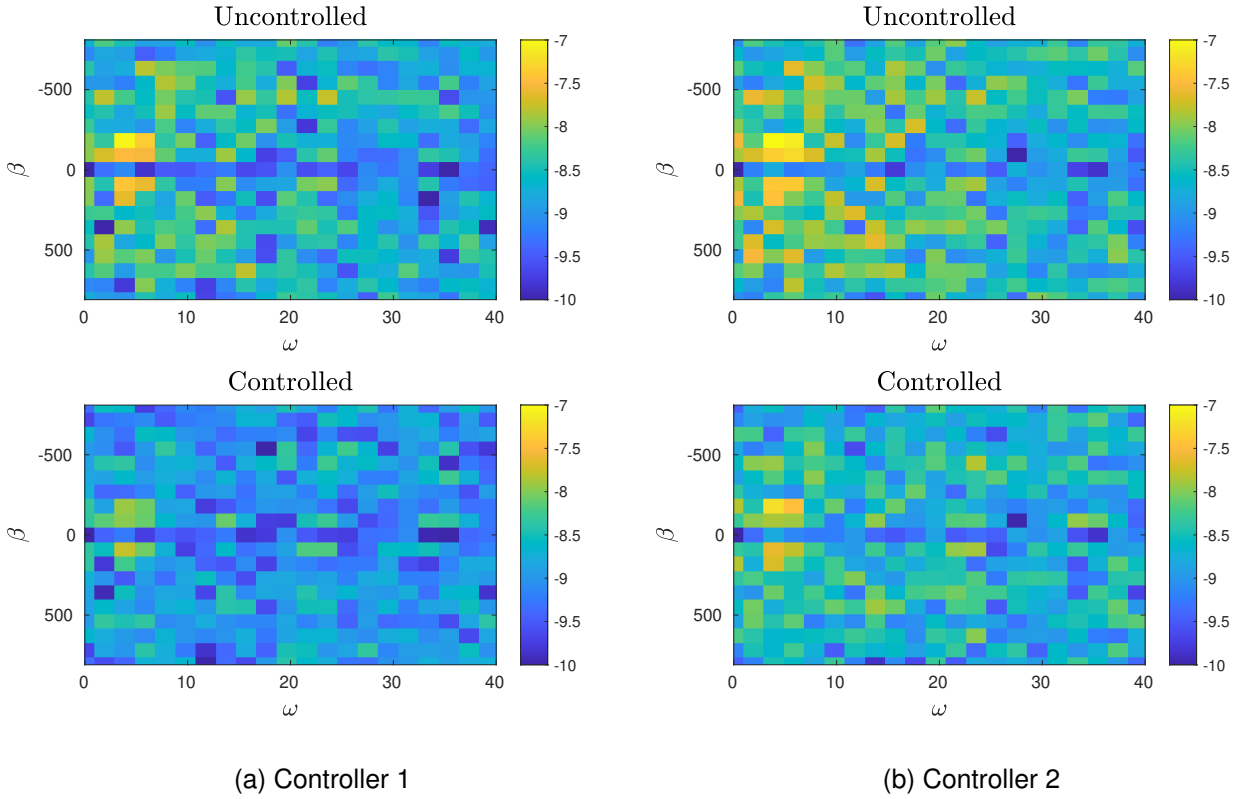(a) Controller 1   (b) Controller 2

Figure 10 – Spectrum of the signals $z(t)_l$ as a function of frequency and spanwise wavenumber at the chord objective locations $x = 0.1$ and $x = 0.15$ for Controller 1 and 2, respectively.

6. Conclusions

The implementation of a controller to damp streaky structures on a wing profile has been studied numerically. Streaks are generated by forcing the wing boundary-layer with synthesised free-stream turbulence, which is built from random Fourier modes following the Von-Kármán spectrum. The controllers have been designed using a data-driven approach, where only wall-measurements are used to mimic an experimental set-up.

The IFFC controller has been proven to be successful in reducing not only the objective function, but also the disturbance amplitude. In particular, for the low-turbulence intensity case the decay of the streaky structures continues downstream of the objective location. When the turbulence intensity is increased to 2.5% the controller is still effective in minimising the objective function and damp the disturbances amplitude. Here, and after the actuation, the controlled $\max(u_{rms})$ in figure 9 grows below the uncontrolled one. However, the disturbance growth recovers downstream, reaching the levels of the uncontrolled case. This behaviour has been observed for the two control units configurations under study.

We conjecture that the poor performance in delaying transition in our flow configuration is due to the controller not being able to damp the streaky structures responsible for the secondary instabilities downstream. Therefore, future work should focus on a different configuration to measure and actuate on these streaks. Some of the alternatives include: the redefinition of the objective function for the controller design, and the number and type of sensors/actuators.
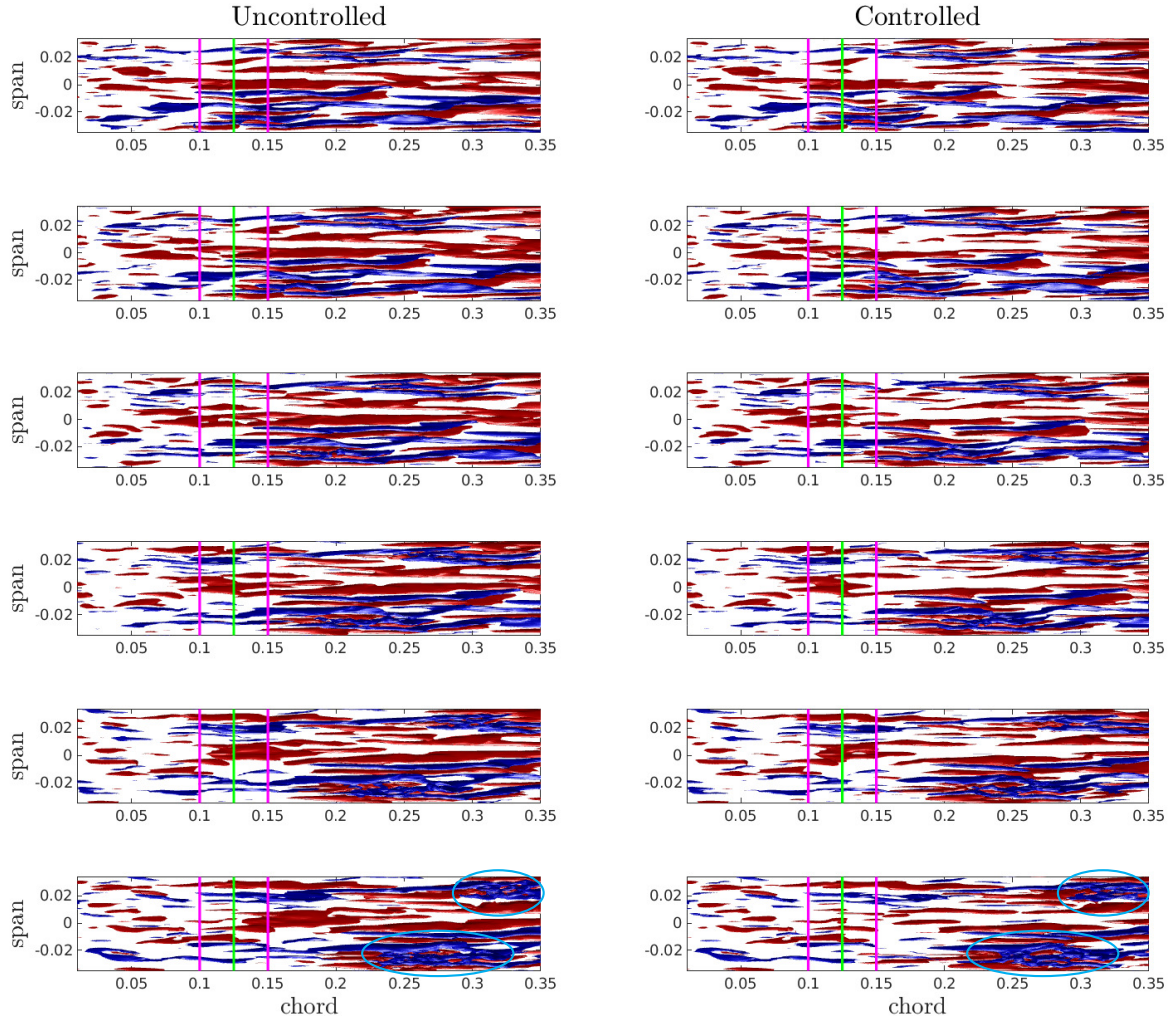
Figure 11 – Snapshots of the perturbed flow field for Uncontrolled (left) and Controller 2 (right) cases, with the isosurfaces (± 0.08) showing the positive (red) and negative (blue) streamwise velocity perturbation. Time increases from top to bottom with a step of $\Delta t = 0.03$ time units. Magenta and green lines show the chord location of sensors and actuators, respectively, while two turbulent spots are enclosed by the cyan lines.

Contact Author Email Address

José M. Faúndez: josfa@kth.se

Acknowledgements

Copyright Statement

References

[1] Schrauf G. Status and perspectives of laminar flow. *Aeronautical Journal*, Vol. 109, No. 1102, pp 639–644, 2005.

[2] Schmid P J and Henningson D S. *Stability and transition in shear flows*. New York, NY: Springer, 2001.

[3] Brito P P, Morra P, Cavalieri A V, Araújo T B, Henningson D S and Hanifi A. Experimental control of Tollmien–Schlichting waves using pressure sensors and plasma actuators. *Experiments in Fluids*, Vol. 62, No. 2, pp 1–13, 2021. URL `https://doi.org/10.1007/s00348-020-03112-4`.

[4] Morra P, Sasaki K, Hanifi A, Cavalieri A V and Henningson D S. A realizable data-driven approach to delay bypass transition with control theory. *Journal of Fluid Mechanics*, Vol. 883, 2019.

[5] Sasaki K, Morra P, Cavalieri A V, Hanifi A and Henningson D S. On the role of actuation for the control of streaky structures in boundary layers. *Journal of Fluid Mechanics*, Vol. 883, 2019.

[6] Fischer P, Kruse J, Mullen J, Tufo H, Lottes J and Kerkemeier S. Nek5000: Open source spectral element CFD solver. *Argonne National Laboratory, Mathematics and Computer Science Division, Argonne, IL, see https://nek5000. mcs. anl. gov/index. php/MainPage*, Vol. 2, 2008.

[7] Negi P. *Stability and transition in pitching wings*. Ph.D. thesis, KTH Royal Institute of Technology, 2019.

[8] Shahriari N, Kollert M R and Hanifi A. Control of a swept-wing boundary layer using ring-type plasma actuators. *Journal of Fluid Mechanics*, Vol. 844, pp 36–60, 2018.

[9] Monokrousos A, Brandt L, Schlatter P and Henningson D S. DNS and LES of estimation and control of transition in boundary layers subject to free-stream turbulence. *International Journal of Heat and Fluid Flow*, Vol. 29, No. 3, pp 841–855, 2008.

[10] Devasia S. Should model-based inverse inputs be used as feedforward under plant uncertainty? *IEEE Transactions on Automatic Control*, Vol. 47, No. 11, pp 1865–1871, 2002.

[11] Bendat J S and Piersol A G. *Random data: analysis and measurement procedures*. John Wiley & Sons, 2011.

[12] Fabbiane N, Bagheri S and Henningson D S. Energy efficiency and performance limitations of linear adaptive control for transition delay. *Journal of Fluid Mechanics*, Vol. 810, pp 60–81, 2017.

[13] Lundell F. Reactive control of transition induced by free-stream turbulence: An experimental demonstration. *Journal of Fluid Mechanics*, Vol. 585, pp 41–71, 2007.